Article

The Role of Cation Coordination in the Electrical and Optical Properties of Amorphous Transparent Conducting Oxides

Sebastian Husein, Julia E. Medvedeva, John D. Perkins, and Mariana I. Bertoni*

Read Online

ACCESS | Metrics & More | Article Recommendations | SI Supporting Information

ABSTRACT: Amorphous oxide semiconductor materials have demonstrated numerous advantages without compromise of electrical properties as compared to their crystalline counterparts, yet understanding of the fundamental principles allowing this has remained elusive. To study the origins of enhanced optoelectronic properties, we apply high-throughput, combinatorial sputtering, structural and spectral mapping, and computationally intensive *ab initio* molecular dynamics simulations with density functional theory to a ternary, post-transition metal oxide system, namely, zinc tin oxide. The deposited thin films exhibit a high figure of merit, achieving carrier densities in the range of 10^{19} to 10^{20} cm^{-3} and carrier mobilities up to 35 cm^2/Vs. These results highlight the role of local distortions and cation coordination in determining the microscopic origins of carrier generation and transport. In particular, we identify the strong likelihood of Sn undercoordination in both Zn-poor and Zn-rich phases leading to the high carrier concentrations observed. This not only diverges from the still widespread historical indictment of oxygen vacancies controlling carrier population in crystalline oxides but also provides a comprehensive framework to describe the unique structure−property relationships using specific structural and electronic descriptors in disordered phase materials.
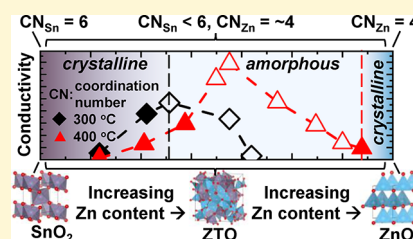
INTRODUCTION

Amorphous oxide semiconductors (AOS) have been increasingly studied in the past two decades, allowing impressive advancements in display, photovoltaic, sensing, computing, communication, and identification technologies.[1−5] Promising AOS materials are the ternary and quaternary amorphous oxides, In−Sn−O (a-ITO), In−Zn−O (a-IZO), In−Ga−Zn−O (a-IGZO), or Zn−In−Sn−O (a-ZITO). Four factors are propelling interest in these materials:

(1) Disorder-driven tunability of optoelectronic properties[6−14]

(2) Uniform, large area depositions[5,15] made possible by low surface roughness[16,17] and enhanced etching uniformity[6,18,19] due to isotropic properties and the lack of grain boundaries in amorphous materials

(3) Enhanced mechanical flexibility and compatibility with diverse, inexpensive substrates[20,21]

(4) Electrical conductivities and carrier mobilities comparable to their polycrystalline counterparts[22−36]

Regarding (4), an overview of electrical properties of best-performing crystalline TCOs and AOS is given by Medvedeva et al.[14] Practical crystalline TCOs can achieve carrier mobilities (μ_e) up to 100 cm^2/Vs with carrier densities (N_e) spanning 10^{19}−10^{20} cm^{-3} (although N_e up to 10^{21} cm^{-3} is possible, μ_e is typically <70 cm^2/Vs in these cases); AOS materials readily achieve μ_e values of 10−60 cm^2/Vs at N_e values of 10^{20} as well. Therefore, the advantages of (1)−(3) are attainable in AOS materials without significant compromise of electrical performance compared to crystalline TCOs.

Since the use of TCO materials covers a broad array of technologies, meaning optical and electrical requirements can vary greatly depending upon specific application, disorder-driven tunability of optoelectronic properties is of particular importance, where coordination and concentration of the (multi)cation species can be a lever to tune material properties.

In particular, improvement of μ_e through structural disorder enhancement has been observed in several oxide systems, including cadmium indium oxide,[37] indium oxide,[14,36,38,39] ZITO,[14] and zinc tin oxide (ZTO).[11,35,40] In the case of indium oxide, several methods have been used to vary structural order of as-deposited thin films: depositing at temperatures below 273 K, and introducing hydrogen during deposition.[36,38,39] Decreasing the temperature or increasing the H concentration during deposition increases the amorphous fraction of the films, with a local maximum in electrical conductivity (σ_e) observed near the transition from crystalline to fully amorphous.[36,39] Interestingly, this increase in σ_e is not solely driven by an increase in N_e, as some authors have posited H to be a donor in many metal oxide systems,[41−49] but complemented by a simultaneously large increase in μ_e.[38,39,50] In prior studies, the amorphous and crystalline structures of

In_2O_3 were investigated by molecular dynamics (MD) simulations and experiments. It was found that the spatial distribution and connectivity of the fully (octahedrally) coordinated In atoms strongly correlate with the MD quench rates applied, i.e., InO_6 polyhedra network arrangement depended upon the crystalline fraction allowed to form upon cooling of the In_2O_3 melt.[36] Based on this, the observed peak in μ_e corresponded to a structure with long chains of the InO_6 polyhedra connected primarily by corner sharing,[36] with the broader implication being that the manner in which a metal–oxygen polyhedra network form plays an essential part in carrier transport in amorphous oxides.[12] The propensity of indium oxide to crystallize at relatively low temperatures,[51] as well as scarcity concerns for continued reliance on indium,[52,53] makes its oxides questionable candidates for high-performance, high-volume AOS application. This motivates one to seek out In-free alternatives with greater amorphous structure stability, e.g., ZTO.

The incorporation of multiple cations in an oxide structure, such as in ZTO, shifts the crystallization temperature, allowing access to amorphous structures across a broader temperature range.[36] However, the microscopic effects of compositional variation in ZTO on local and long-range order and on transport properties—carrier generation, N_e, and μ_e—are unclear. Studies of ZTO have primarily been in developing ZTO as a thin-film transistor or buffer layer for device incorporation,[17,27,40,54−61] post-deposition treatments,[62−64] or in developing low-cost, low-temperature growth methods.[65−67] Only recently have some authors begun to inspect the origins of transport properties from an electronic structure view of ZTO.[11,35,40,68−73] Many of these studies consider a narrow range of ZTO compositions, investigate ZTO films with carrier densities lower than those suitable for widespread optoelectronic applications, or do not satisfactorily provide information on the local coordination changes of atomic species with changing metal composition. In this study, we use a combinatorial sputtering approach for deposition and characterization of ZTO spanning 100% SnO_2 to 100% ZnO with compositional libraries containing a large set of varied Zn:Sn ratios, sputtered at 300 and 400 °C, resulting in films with optoelectronic device-relevant electrical performances. The experimental observations are paired with *ab initio* MD simulated structures to determine the origin of transport properties via a thorough analysis of the structural characteristics and accurately calculated electronic and optical properties of the disordered Zn−Sn−O with variable metal composition.

EXPERIMENTAL METHODS

Zn−Sn−O thin films were co-sputtered using a two-gun RF magnetron without rotation to obtain compositional libraries across 8×8 cm substrates. AF-32 Schott glass substrates from Howard Glass Co. were mounted on a heated substrate holder facing two ceramic targets of ZnO and SnO_2.

Substrate temperature was monitored using a k-type thermocouple mounted at the back surface of the substrates. Deposition temperatures used were 300 and 400 °C. The chamber was evacuated to 1.3×10^{-5} to 2×10^{-4} Pa prior to deposition, with a 20 sccm flow of Ar at 0.8 Pa working pressure during deposition. Three powers were selected per target: SnO_2: 2.22, 3.33, and 4.88 W/cm²; ZnO: 1.63, 2.51, and 3.26 W/cm². Six depositions by sputtering only from one target at the above powers were made to evaluate the pure SnO_2 film and pure ZnO film thickness as a function of location on the substrate. Before sputtering, masking lines were drawn at constant

increments across the 8×8 cm substrates. After sputtering, these lines defined clear film thickness step heights that were evaluated by a Bruker DektakXT profilometer with an automated stage assembly.

Using both targets at the nine combinations of powers above, combinatorial sputtering allowed different locations on the substrate to achieve different Zn:Sn ratios due to varied thickness mixing. Across the substrates, regions with $[Zn]/([Sn]+[Zn]) = 4–97\%$ were obtained. Sputtering from a single target provided $[Zn]/([Sn]+[Zn]) = 0$ and 100% films. By measuring the thickness gradient across the substrate from a deposition of only ZnO and the thickness gradient from a subsequent deposition of only SnO_2, the composition gradient across the substrate surface area was estimated, assuming sputtering rates remained approximately the same when co-sputtering from two targets as when sputtering from single targets.

Film thicknesses of the co-sputtered films were evaluated by the masking procedure mentioned above, and profilometer measurements showed a <20 nm delta of the co-sputtered ZTO film thickness from the sum of the ZnO-only film thickness + SnO_2-only film thickness. ZTO films deposited varied in thickness from 120 to 370 nm across the substrate surface, resulting in the composition gradient.

The 8 cm × 8 cm substrate was cut into 1 cm × 1 cm pieces for further evaluation. Film thickness variations across these 1 cm × 1 cm pieces were <20 nm, and resulting calculated composition variations across the smaller, scribed films were <3 atomic % absolute. The calculated compositions from selected areas of the ZTO films were confirmed by Rutherford backscattering (RBS) using a 1.85 MeV He ion beam in the facilities of the University of Michigan Ion Beam Laboratory (MIBL). The RBS-measured $[Zn]/([Sn]+[Zn])\%$ values were all <5 atomic % absolute from the estimated $[Zn]/([Sn]+[Zn])\%$. These estimated $[Zn]/([Sn]+[Zn])$ values were calculated from the film thicknesses according to

$$[Zn]/([Sn] + [Zn]) = \frac{\frac{T_{ZnO}}{N_{Zn}}}{\frac{T_{ZnO}}{N_{Zn}} + \frac{T_{SnO_2}}{N_{Sn}}} \tag{1}$$

where T_{Zn} and T_{SnO_2} are the film thickness of ZnO and SnO_2, respectively, and N_{Zn} and N_{Sn} are the number of Zn atoms and Sn atoms per volume unit cell, respectively, calculated from an estimated ZnO density of 5.6 g/cm³ and atomic weight 81.38 and SnO_2 density of 6.9 g/cm³ and atomic weight 150.71.

Electrical properties of the films were characterized and compared by both four-point probe and Hall effect. An automated four-point probe system was used to map the resistivity of 1024 points across the 8 cm × 8 cm samples prior to scribing. After scribing, Hall effect measurements were taken in the standard van der Pauw configuration using an Ecopia HMS-3000 at room temperature, where Ohmic contact was established by using thermally evaporated Au/Ti contacts on the corners of the scribed films. For ZTO films deposited at 300 and 400 °C, conductivities were measured separately by four-point probe and Hall effect. The separately measured conductivities agreed within 20% of each other for films with $[Zn]/([Sn]+[Zn]) = 20–55\%$ and $[Zn]/([Sn]+[Zn]) = 20–75\%$, respectively. Polarity of the Hall measurements (i.e., observing the Hall voltages with different square contact configurations) was found to vary no more than a relative ~10% on a given sample, indicating the sample dimensions (e.g., thickness) and composition gradient across the 1 cm × 1 cm samples did not significantly impact measurements. To provide some measure of uncertainty/measurement error, duplicate deposited films were measured by Hall effect for these compositions; the reported four-point probe and Hall effect electrical properties are the averages for 3−5 films measured multiple times each at a given composition (i.e., position on the 8 cm × 8 cm substrate).

For ZTO films deposited at 300 °C with $[Zn]/([Sn]+[Zn]) = <20$ and >55% and deposited at 400 °C with $[Zn]/([Sn]+[Zn]) = <20\%$ and >75%, Hall measurement results appear unreliable due to high standard deviations between samples, potentially coming from observed non-Ohmic contact (characterized by non-linear current vs voltage sweeps) despite similarly evaporated Au/Ti contacts, or from more rapidly spatially changing composition and thickness
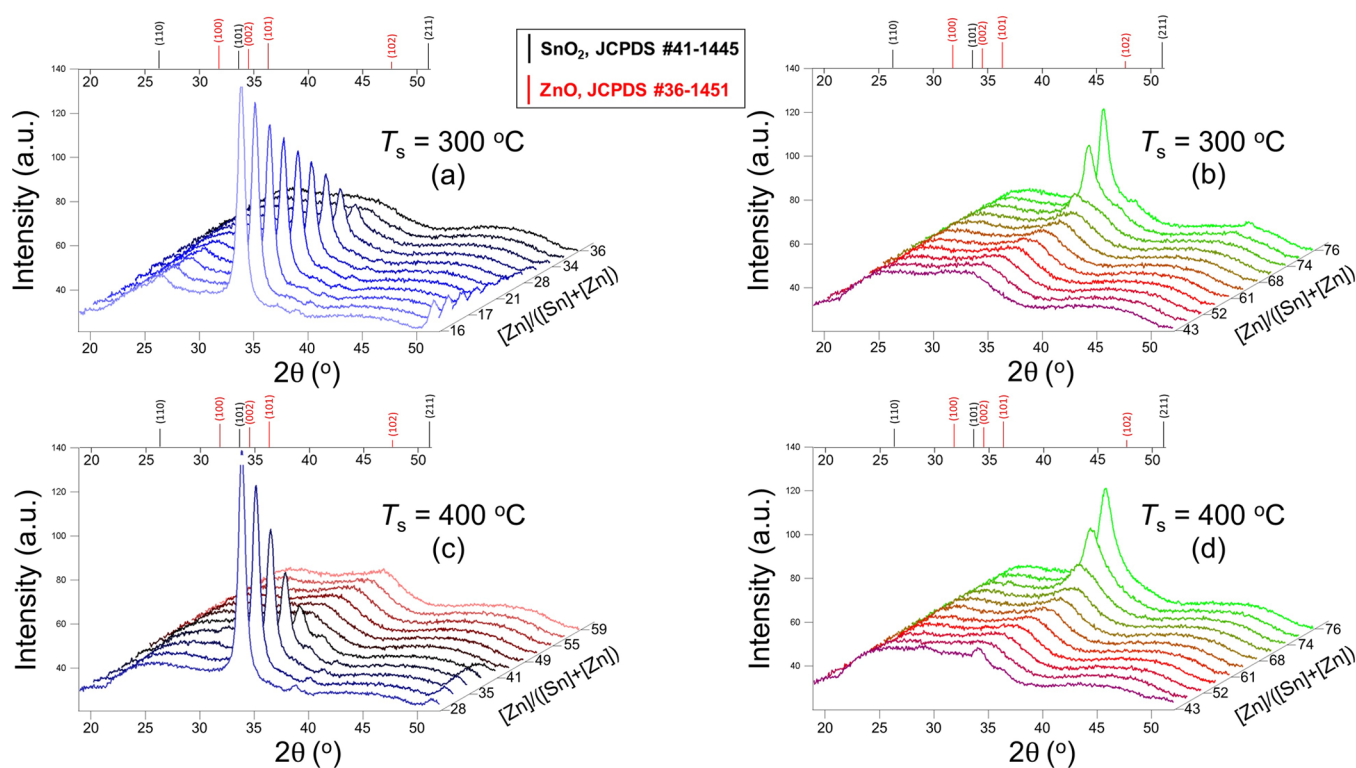
Figure 1. X-ray diffraction spectra of ZTO films grown at 300 and 400 °C for (a, c) low Zn% and (b, d) high Zn%.

across the 1 cm × 1 cm samples due to their positions closer to the edges of the 8 cm × 8 cm substrate. The resistivities of these films from Hall effect measurements were additionally >20% larger or smaller than the four-point probe resistivity measurements. Only the four-point probe resistivity (conductivity) values are therefore reported here for these films. The exception to this are the uniformly deposited 100% SnO_2 and 100% ZnO samples, grown by single-target sputtering at 300 and 400 °C.

Phase analysis was done in a Bruker ASX D8 X-ray diffractometer (Bruker ASX Inc., WI, USA) and PANalytical X'Pert PRO MRD, both with a Cu anode. Standard 2θ scans were taken between 18° and 52° at 0.02° steps in the Bruker, while scans from 15° to 85° were taken in the PANalytical on select films of low Zn% content.

Ab initio MD simulations of the crystalline and amorphous ZTO lattices, detailed in a later section, were used to inspect coordination of the cations as well as origins of carrier generation and carrier density.

◼ EXPERIMENTAL RESULTS

Structural Order of Zinc Tin Oxide Films. ZTO films grown at T_s = 300 and 400 °C are shown in Figure 1. The diffraction peaks of these as-deposited films can be indexed by standard peaks of rutile tin oxide (JCPDS #41-1445) and wurtzite zinc oxide (JCPDS #36-1451). Figure 1a,b shows ZTO grown at T_s = 300 °C with compositions [Zn]/([Sn]+[Zn]) = 16% < x < 37% and [Zn]/([Sn]+[Zn]) = 43% < x < 77%, respectively. Figure 1c,d shows ZTO grown at T_s = 400 °C with compositions [Zn]/([Sn]+[Zn]) = 28% < x < 59% and [Zn]/([Sn]+[Zn]) = 43% < x < 77%, respectively. X-ray diffraction (XRD) scans of the full compositional range are provided in the Supporting Information.

Figure 1a with [Zn]/([Sn]+[Zn]) = 16% < x < 37% shows the (110), (101), and (211) of SnO_2 with a preferential growth in the (101) for [Zn]/([Sn]+[Zn]) ≤ ~34%. A transition from crystalline to fully X-ray amorphous above ~34% [Zn]/([Sn]+[Zn]) is observed for T_s = 300 °C.

For T_s = 400 °C shown in Figure 1c, the (101) and (211) of SnO_2 are observed for [Zn]/([Sn]+[Zn]) <41%, with a transition from crystalline to amorphous then occurring above [Zn]/([Sn]+[Zn]) =

43% seen in Figure 1d. For both T_s values, a transition from fully amorphous to crystalline exists near 74% [Zn]/([Sn]+[Zn]), as seen in Figure 1b,d. The XRD spectra observed after this transition at a high [Zn]/([Sn]+[Zn]) % show a broad peak near 32.5° 2θ, which is not immediately identifiable by either SnO_2 or ZnO standards. This main peak appears to correspond to the (311) of the cubic inverse spinel Zn_2SnO_4 structure according to JCPDF #24-1470;[74−76] however, substrate temperatures of T_s = 300 and 400 °C make it unlikely for Zn_2SnO_4 to form during sputtering. Young *et al.* and Wu *et al.* obtain the cubic spinel structure only upon annealing at temperatures above 600 °C[74−76] (after sputtering either without intentional heating of the substrate or T_s >550 °C). From a thorough review of ZTO synthesis procedures from Sun and Liang,[77] it is seen that Zn_2SnO_4 can be grown by thermal evaporation at 800−1000 °C and by electrospinning followed by calcination at 700 °C, among other methods, supporting the unlikelihood of Zn_2SnO_4 being present in these films.

To identify this peak occurring near 2θ = 32.5°, several diffraction spectra were taken with different tilts around the torsion angle, χ, of the highest Zn content ([Zn]/([Sn]+[Zn]) = 76%) film where this peak is most prominent. These measurements taken at four distinct χ tilts are shown in the Supporting Information. At χ = 90° and 60°, the peak near 2θ = 32.5° is still observed with decreasing intensity as χ increases. At χ = 45°, this peak is significantly diminished, and peaks at 2θ = ~35.3°, ~46.2°, and ~56° begin to appear, consistent with the expected (101), (102), and (110) of the wurtzite ZnO structure (JCPDS #36-1451). At χ = 30°, a clear intensity peak lies at the same angle as the (101) of ZnO, with the (102) and (110) peaks also slightly visible.

Optical Absorption. By inspecting the absorption coefficient in the short wavelength regime, information about the band edges can be obtained. The absorption coefficient is calculated from measurements of transmittance and reflectance, according to[78]

$$\alpha = \frac{-1}{d}\ln\left(\frac{T}{1-R}\right) \tag{2}$$

where d is the film thickness in nm, T is the transmittance, and R is the reflectance. Figure 2 shows α in cm^{-1} for eight depositions, each
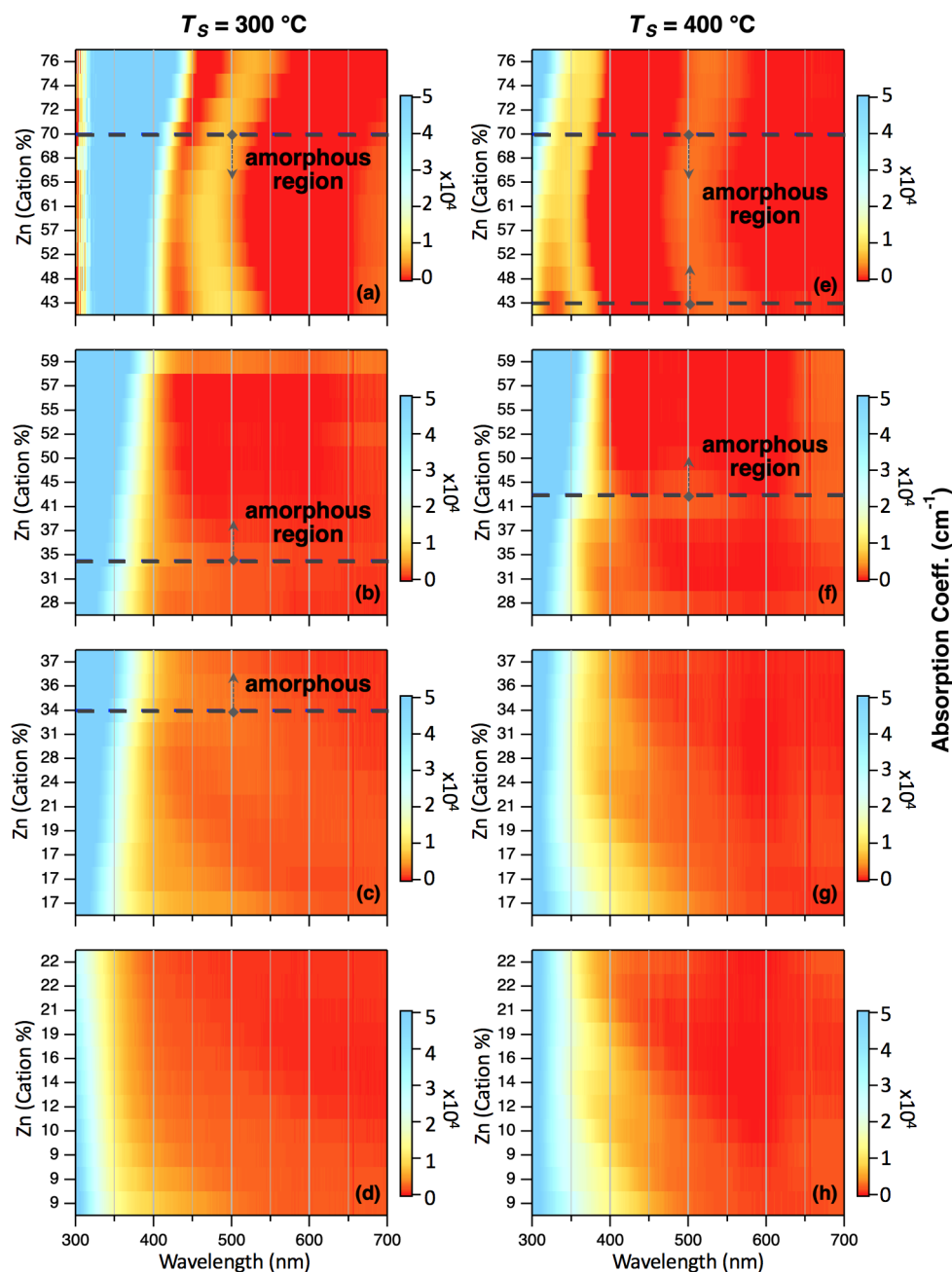
Figure 2. Absorption coefficients of ZTO films grown at (a–d) 300 °C and (e–h) 400 °C. The gray dashed lines indicate the bound of the composition range over which the sputtered films were measured as fully X-ray amorphous: in (a), $[Zn]/([Sn]+[Zn]) < 70\%$; in (b) and (c), $[Zn]/([Sn]+[Zn]) > 34\%$; in (e), $43\% < [Zn]/([Sn]+[Zn]) < 70\%$; and in (f), $[Zn]/([Sn]+[Zn]) > 43\%$.

with a composition range that overlaps with the preceding and succeeding deposition. The range of this overlap increases with increasing Zn content.

Regions of low absorption are seen in red, and blue indicates regions of higher absorption. The maximum visible transmission window occurs near 61% Zn for both $T_s = 300$ and 400 °C, as seen in Figure 2a,e. The visible wavelength transmission window for both $T_s = 300$ and 400 °C narrows with increasing Zn% until a discontinuity near 42.5% Zn for the sample deposited with the highest Zn content. For $T_s = 400$ °C films, extended absorption into the visible range is seen, particularly for a low Zn content of ≤37%. These absorption tails appear more strongly for the films at 400 °C than those deposited at 300 °C.

The decreasing optical band gap with increasing Zn% affirms calculated optical absorption information. Calculated absorption coefficients (shown later in Figure 7d) indicate that the band gap is

larger for $[Zn]/([Sn]+[Zn]) = 30\%$ than for $[Zn]/([Sn]+[Zn]) = 44$ and 59%.

A discontinuity of the absorption coefficient occurs between the composition range of ∼42.5–59.5 Zn% as there is a composition overlap between samples sputtered at different SnO$_2$ and ZnO target powers. A similar discontinuity is seen for the $T_s = 300$ °C film between ∼17 and 22.5 Zn%, and less pronounced discontinuities at ∼27–37 Zn% and ∼42.5–59.5 Zn%. These discontinuities indicate that more than composition was altered by deposition conditions and may result from non-uniform film thicknesses unaccounted for when calculating α.

In the fully amorphous composition range, a broadening of the visible wavelength transmission window is observed for both deposition temperatures between ∼57 and 65 Zn%, with a maximum transmission near 61% Zn.

A full discussion of these absorption features can be made in concert with the carrier population behavior of these films and will therefore follow after presenting the electrical properties.

Figure 3 shows the σ_e, N_e, and μ_e of the ZTO films deposited at two substrate temperatures as a function of Zn content as well as a
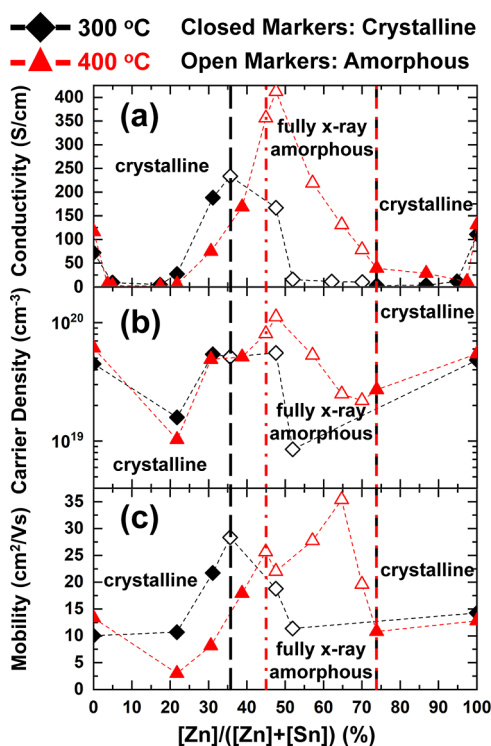

Figure 3. Room temperature electrical properties of ZTO deposited at T_s = 300 or 400 °C. (a) Conductivity measured by four-point probe. (b) Carrier density and (c) carrier mobility measured by Hall effect. Measurement uncertainty contained within the marker size. Solid markers indicate partially crystalline films; open markers indicate fully X-ray amorphous films. Black vertical, long-dashed lines and red dashed-dotted lines indicate a phase transition point of crystalline to amorphous for 300 °C-grown films and 400 °C-grown films, respectively. Both 300 °C samples with [Zn]/([Sn]+[Zn]) = <20 and >55% and 400 °C samples with [Zn]/([Sn]+[Zn]) = <20 and >75% could not be reliably measured by Hall effect; therefore, only four-point probe conductivity values are reported in (a).

representation of the structural order of each sample provided by the XRD measurements of the prior section. Closed markers indicate that diffraction peaks are observed in the XRD spectra, signifying at least partial crystallinity in the film bulk, while open markers indicate fully X-ray amorphous films. The crystalline regions occur to the left of the vertical, dashed lines shown at [Zn]/([Sn]+[Zn]) = 35.6% (in black, for films grown at T_s = 300 °C), [Zn]/([Sn]+[Zn]) = 45% (in red, for films grown at T_s = 400 °C), and to the right of the overlapping vertical, dashed lines at [Zn]/([Sn]+[Zn]) = 70.7% (films grown at T_s = 300 and 400 °C). Films in the regions between these are fully X-ray amorphous. Starting at a low Zn content, the increase in Zn into SnO$_2$ leads to a monotonic increase in σ_e until a maximum value, occurring near the indicated transitions from crystalline to amorphous.

Figure 3 shows the maximum σ_e increases and shifts to higher Zn contents with increasing T_s. For T_s = 300 and 400 °C, the maximum conductivities are σ_e = ~233 and ~394 S/cm, respectively. These occur at [Zn]/([Sn]+[Zn]) = 35.6 and 47.6 atomic %.

For films deposited at T_s = 300 °C, the maximum μ_e of 28.4 cm^2/Vs occurs at the same [Zn]/([Sn]+[Zn]) = 35.6% as the σ_e maximum, while N_e remains relatively flat through the entire range of 31.1–47.6% [Zn]/([Sn]+[Zn]).

Films deposited at T_s = 400 °C exhibit a different behavior. The maximum σ_e coincides with the maximum N_e of ~1.1 × 10^{20} cm^{-3} at [Zn]/([Sn]+[Zn]) = 47.6%, whereas two local carrier mobility maxima occur at [Zn]/([Sn]+[Zn]) = 44.9% and [Zn]/([Sn]+[Zn]) = 64.7%. These mobility maxima occur relatively close to the order–disorder transition points observed in the XRD spectra. The 300 °C transitions points observed were at [Zn]/([Sn]+[Zn]) >34 and <70%, while the 400 °C transition points observed were at [Zn]/([Sn]+[Zn]) >43% and <70%.

Composition. Zinc, tin, and oxygen contents of the films were evaluated by ion beam analysis, specifically RBS. From these measurements, the film density is simultaneously obtained. The measured oxygen content and film density are shown in Figure 4.
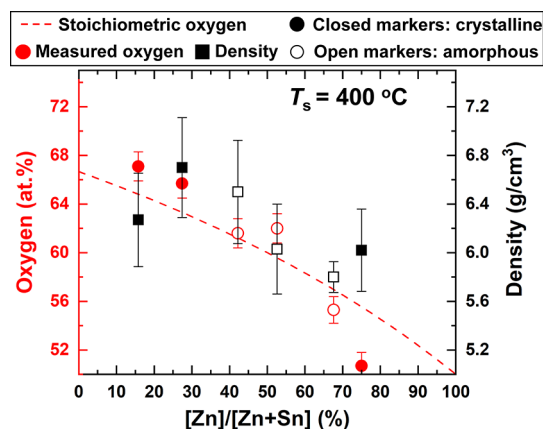

Figure 4. Oxygen content (red circles) and film densities (black squares) measured by Rutherford backscattering of zinc tin oxide films grown at 400 °C. Closed markers indicate that the films are partially crystalline, while open markers indicate that the films are fully X-ray amorphous. The red dashed line is the calculated stoichiometric oxygen atomic % for a given [Zn]/([Zn]+[Sn]) %.

While [Zn]/([Sn]+[Zn]) % values of Figure 3 are estimates based on measured film thicknesses and calculated according to eq 1, [Zn]/([Sn]+[Zn]) % values of Figure 4 are from the RBS measurements. A table providing a comparison of the values is given in the Supporting Information. The largest absolute % difference is <5% between the calculated and measured [Zn]/([Sn]+[Zn]) values.

The stoichiometric oxygen atomic % is calculated as a function of [Zn]/([Sn]+[Zn]). The resulting curve is shown in Figure 4 as a red dashed line, with the measured O atomic % and calculated stoichiometric O atomic % values indicated by the left y axis. It is seen in Figure 4 that the absolute oxygen content decreases with increasing Zn content; however, the films are overstoichiometric up to the film measured with [Zn]/([Sn]+[Zn]) = 52.6%. The films with [Zn]/([Sn]+[Zn]) = 68.2 and 75.5% are substoichiometric.

Estimates of the bulk film density are also shown in Figure 4, with values indicated by the right y axis. Note that limitations of RBS detector sensitivity for lighter elements such as oxygen result in relatively large uncertainties of the estimated film densities. An increase in film density is observed at [Zn]/([Sn]+[Zn]) = 28.6% as crystallinity of the films decreases followed by a decrease in film density after the transition to completely X-ray amorphous. Upon transitioning back to crystalline at ~70%, a slight increase in film density is observed again. However, these film density changes are all within the uncertainty of each other.

Theoretical Methods. To understand the observed electrical behavior as it relates to the structural order, particularly for amorphous films, amorphous binary and ternary Zn–Sn–O structures were generated using first-principles molecular dynamics (MD) liquid-quench simulations as implemented in the Vienna ab initio simulation package (VASP).[79−83] The calculations were based on density functional theory (DFT) within the generalized gradient

approximation with the Perdew–Burke–Ernzerhof (PBE) functional[84] and with periodic boundary conditions.

Initial randomized cells were constructed: ZTO30 = 146-atom $Zn_{16}Sn_{38}O_{92}$, with density 6.407 g/cm^3; ZTO44 = 138-atom $Zn_{24}Sn_{30}O_{84}$, with density 6.212 g/cm^3; and ZTO59 = 130-atom $Zn_{32}Sn_{22}O_{76}$, with density 6.016 g/cm^3; as well as $Sn_{46}O_{92}$, with density 6.801 g/cm^3, and $Zn_{70}O_{70}$, with density 5.48 g/cm^3. Note that the density in Zn–Sn–O cells is about 5% lower than the corresponding linear interpolation based on the respective ratio of the crystalline densities, i.e., 6.95 g/cm^3 for SnO$_2$ and 5.61 g/cm^3 for ZnO. These densities are in excellent agreement with our experimental results (Figure 4). To model oxygen substoichiometry, the oxygen content was reduced at the melting stage and was set to correspond to oxygen defect concentrations of 6×10^{20} cm^{-3} ($Sn_{46}O_{91}$, $Zn_{16}Sn_{38}O_{91}$, $Zn_{24}Sn_{30}O_{83}$, $Zn_{32}Sn_{22}O_{75}$, and $Zn_{70}O_{69}$) and 1.2×10^{21} cm^{-3} ($Sn_{46}O_{90}$, $Zn_{16}Sn_{38}O_{90}$, $Zn_{24}Sn_{30}O_{82}$, $Zn_{32}Sn_{22}O_{74}$, and $Zn_{70}O_{68}$) in all compositions.

All initial structures were first melted at 3000 K for at least 10 ps in order to ensure a fully randomized configuration and to stabilize the total energy. Next, liquid-quench simulations were performed by cooling each structure to 2500 K at an MD rate of 100 K/ps then rapidly quenching to 100 K at a 200 K/ps rate. An energy cutoff of 260 eV and a single Γ-point method were used during melting and quenching processes. Next, each structure was equilibrated at 300 K for 6 ps with a cutoff energy of 400 eV. All MD simulations for amorphous oxides were carried out in the NVT ensemble with a Nosé–Hoover thermostat using an integration time step of 2 fs. For accurate structural analysis of both crystalline and amorphous oxides, the room temperature configurations obtained from MD simulations at 300 K (3000 MD steps resulting in 3000 atomic configurations for each structure) were used. The resulting pair correlation functions are shown in the Supporting Information. The average effective coordination number and average bond length were calculated according to refs 85 and 86 and Eqs 1 and 2 in ref 87 for each atom in each MD configuration and then averaged over the 3000 steps (6 ps).

Next, each of the atomic configurations obtained from the *ab initio* MD liquid-quench simulations was optimized within DFT using the PBE functional. For the optimization, the cutoff energy of 500 eV and the 4 × 4 × 4 Γ-centered k-point mesh were used; the atomic positions were relaxed until the Hellmann–Feynman force on each atom was below 0.01 eV/Å. The electronic and optical properties of the PBE-optimized structures were calculated using the hybrid Heyd–Scuseria–Ernzerhof (HSE06) approach[88,89] with a mixing parameter of 0.25 and a screening parameter α of 0.2 Å^{-1}. Note that only the electronic self-consistent calculations were performed in HSE06, whereas the atomic positions were not relaxed. Bader charge analysis in the Voronoi volume around each atom[90] was performed for the conduction states. We argue that the Bader charge calculations provide a much more accurate analysis of the electronic properties in disordered oxides with strong polyhedral distortions than the density of states (DOS) analysis that employs a fixed cutoff radius around atoms to calculate the atomic contributions. Such DOS analyses neglect non-uniform charge distributions. Finally, optical absorption was derived from the frequency-dependent dielectric function, $\varepsilon(\omega) = \varepsilon_1(\omega) + i\varepsilon_2(\omega)$, calculated within the independent particle approximation as implemented in the VASP. The imaginary part, $\varepsilon_2(\omega)$, is related to the optical absorption at a given frequency ω and is determined based on the electronic transitions of the hybrid functional solution. The real part of the complex dielectric function is obtained using Kramers–Kronig relations. The atomic structures and charge densities were plotted using VESTA software.[91]

***Ab Initio* MD Simulations and Property Calculations.** First, we compare the calculated effective coordination numbers (CN) for Sn and Zn in the first shell for simulated amorphous binary and ternary Zn–Sn oxides with different Zn:Sn ratios. The results, shown in Figure 5, reveal that, at room temperature and over the considered range of compositions, the coordination of tin species exhibits a broad distribution, skewed with a significant fraction undercoordinated (CN < 5) as seen in Figure 5a. In contrast, Zn species show a strong preference for its wurtzite tetragonal coordination with a uniform
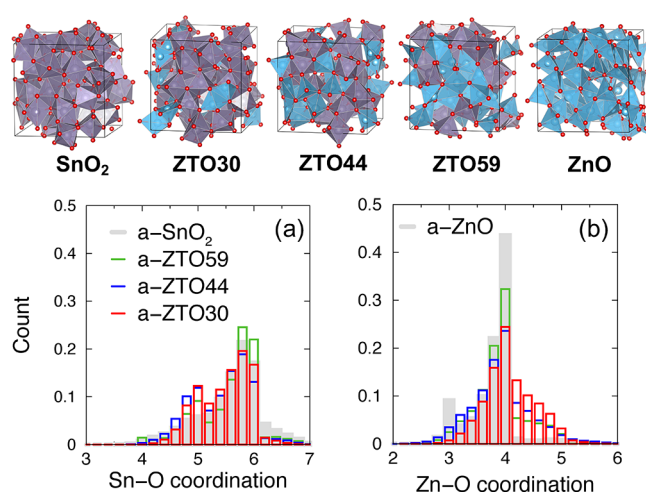

Figure 5. Simulated amorphous structures of binary and ternary Sn–Zn oxides, with 30, 44, and 59% Zn (atomic %) are shown, giving the coordination distribution for (a) Sn species coordinated by O and (b) Zn coordinated by O. The results are from MD simulations at 300 K for 6 ps for the structures with one oxygen defect.

distribution with respect to CN = 4, as seen in Figure 5b. The increasing (decreasing) Zn (Sn) concentration in amorphous Zn–Sn–O suppresses the high-coordinated Zn (CN > 4), whereas for Sn, there are no clear trends observed. Importantly, for both Sn and Zn, the largest fraction of undercoordinated metals is found for ZTO44. This signifies that a nearly equal fraction of Zn and Sn produces the highest number of free carriers, in excellent agreement with our experimental measurements (Figure 3).

The average coordination for Sn and Zn with oxygen and the coordination time variance are shown in Figure 6 for the ZTO
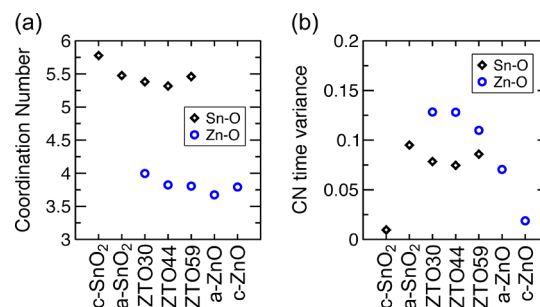

Figure 6. (a) Calculated average Sn and Zn coordination by oxygen in crystalline and amorphous SnO$_2$ and ZnO and in ZTO structures with 30, 44, and 59% Zn. (b) Calculated time variance of the coordination of Sn and Zn. The results are based on the MD simulations at 300 K for the structures with one oxygen defect.

structures with one oxygen defect (the results for the stoichiometric case and non-stoichiometric case with two oxygen defects are given in a table in the Supporting Information). The results are obtained from MD simulations for 6 ps at 300 K so that the variance determines how the CN deviates from the average value within the 6 ps time period. The coordination of Sn decreases with increasing Zn content up to 59% Zn in ZTO, which sees a slight increase in Sn coordination to a similar value as that of the completely amorphous pure SnO$_2$ with an average CN of 5.5 (Figure 6a).

Unlike the Sn species, Zn remains nearly fully coordinated (CN > 3.8) in all ZTO structures, having a higher average coordination than that in amorphous and even crystalline binary ZnO at room temperature, as observed in Figure 6a. At the same time, the coordination variance is notably greater for Zn than for Sn (Figure 6b). It has been shown that the coordination time variance plays a key

role in amorphization.[14] Indeed, the higher CN variance for Zn explains why a large concentration of Zn (>45%) is required to achieve a fully amorphous phase in ZTO grown at 400 °C, making the amorphous region shifted toward Zn-rich phases (Figures 1 and 3).

Based on the calculated electronic properties of amorphous Zn–Sn–O, Bader charge contributions from individual atoms to the conduction band-like state are determined. It is found that Sn contributions are significantly higher than those from Zn, even at 59% Zn incorporation into the ZTO structure (Figure 7a). The charge in
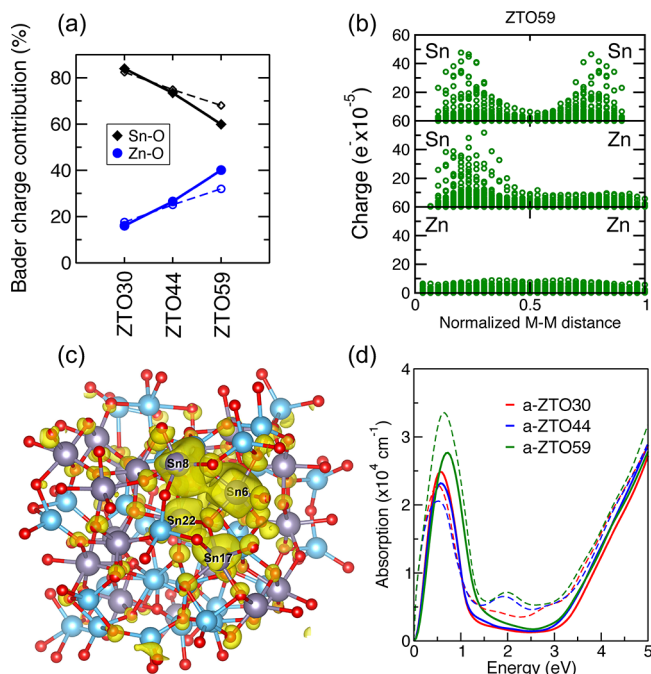

Figure 7. (a) Calculated percentage contribution from Sn and Zn species to the Bader charge in the conduction band-like state that crosses the Fermi level in three ZTO phases with one (solid line) or two (dashed line) oxygen defects. (b) Calculated conduction band charge along metal–metal pairs in ZTO59. (c) Charge density distribution in the conduction states for ZTO59. (d) Calculated optical absorption in three ZTO phases. Solid (dashed) lines represent an oxygen defect concentration of 6 (12) $\times 10^{20}$ cm^{-3}.

the conduction state calculated along all possible metal–metal pairs in ZTO59 (Figure 7b) confirms the localization of the conduction electrons near Sn atoms and also reveals that major contributions come from a few Sn atoms that are undercoordinated (CN = 4.5, 5.0, and 5.1). These low-coordinated Sn atoms cluster in the ZTO59 structure as seen from the calculated charge density distribution (Figure 7c). Such clustering of undercoordinated, undershared metal atoms represents the presence of an oxygen defect in amorphous structures.[14] Therefore, the above results suggest that Sn states are primarily responsible for carrier generation and transport in Zn–Sn–O.

The calculated optical properties, shown in Figure 7d, suggest that at low oxygen deficiency, i.e., for oxygen defect concentrations of 6 × 10^{20} cm^{-3} or below, amorphous Zn–Sn–O structures exhibit low absorption within the visible range; ZTO30 has the largest optical gap. Higher oxygen deficiencies, i.e., oxygen defect concentration of 1.2 × 10^{21} cm^{-3} or above, result in deep localized states that increase the absorption near 2 eV for Zn fractions of 44 and 59% in ZTO. The formation of deep localized states may explain the observed absorption near 500 nm in samples grown at 300 °C, whereas a higher deposition temperature helps to attain more uniform amorphous films with delocalized states, higher carrier concentration, and hence wider optical transmission window, as seen in Figure 2.

From the MD-generated structures, the number of face-, edge-, and corner-shared polyhedra can be evaluated. A representative structure of ZTO with 59% Zn obtained using a quench rate of 200 K/ps is given in Figure 8a, with the calculated distribution of each M−O polyhedra-sharing type in Figure 8b.
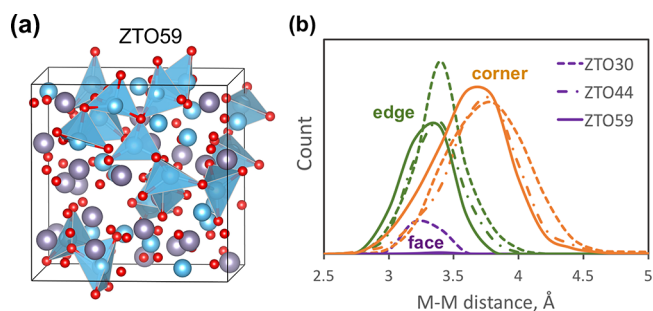

Figure 8. (a) Structure of ZTO with 59% Zn simulated using a quench rate of 200 K/ps. (b) Distribution of face-, edge-, and corner-shared Zn−O polyhedra for 30, 44, and 59 Zn in ZTO for the structures with one oxygen defect.

As seen in Figure 8b, the number of face-sharing polyhedra is suppressed entirely, while the number of edge-shared polyhedra and the distance between such polyhedra are both reduced as Zn content increases from 30 to 59%. Simultaneously, the number of corner-shared polyhedra increases also with the M−M distance reducing. These results are in agreement with tetragonally coordinated Zn preferring corner-sharing configurations. From these observations, it is evident that Zn controls the medium-range structure and governs film morphology, which affects carrier mobility. Based on the polyhedra-sharing distributions, the most uniform morphology is expected to occur for ZTO59; indeed, the observed mobility is the highest for 60−65% Zn.

■ DISCUSSION

In Figure 1b,d, a peak not indexed by the standard peaks of rutile SnO$_2$ (JCPDS #41-1445) and wurtzite ZnO (JCPDS #36-1451) was observed. Upon further inspection, we identified this peak as ZnO (101) with a slight offset to smaller 2θ values. A similar broad peak was observed at $2\theta = $ ~33° by Hayashi et al. and Moriga et al.[92,93] While these authors did not explain the nature of the peak, they showed an unambiguous wurtzite ZnO (002) diffraction peak at an immediately higher composition ([Zn]/([Sn]+[Zn]) = ~80%).[92,93]

A possible explanation for the existence of this broad, shifted (101) peak in Figure 1b,d could relate to local order in the amorphous phase. If the transition from amorphous to crystalline involves a gradual phase change from the trigonal ilmenite-like phase (ZnSnO$_3$) to the wurtzite one (ZnO), then it is possible that, at those transitional compositions, a percentage of zinc exists with a coordination number of 4 in a wurtzite-like structure. This is consistent with a prior work, which has shown that local cation coordination environments are preserved due to strong metal-to-oxygen charge transfer despite long-range structural disorder in amorphous oxides.[8] When tin is introduced into the matrix, the tetragonally coordinated cation induces an expansion of the lattice. This allows observation of the ZnO structure when tilting in χ, but with the characteristic peaks offset to smaller 2θ angles. From this, we conclude that a significant amount of the ZnO phase exists in the partially crystalline films with [Zn]/([Sn]+[Zn]) ≥ 70% and also exists in the amorphous films at a lower [Zn]/([Sn]+[Zn])%.

The optical absorption data of Figure 2 supports the existence of a significant ZnO fraction in the amorphous ZTO films. The visible wavelength transmission window for both T_s = 300 and 400 °C narrows with increasing Zn%, as seen in Figure 2b,c,f–h. This is consistent with the picture of a monotonically decreasing band gap as the films transition from pure SnO_2 to pure ZnO. Band gaps of 3.7–3.4 eV are attributed to rutile SnO_2,[94−100] while band gaps of 3.2–3.43 eV are attributed to wurtzite ZnO.[97,101−104] Perkins et al. show that the optical band gap of sputtered Zn_2SnO_4 is wider than that of ZnO.[102]

As seen in Figure 1a,c, we observe the crystalline-to-amorphous-order transition point for the 400 °C films shifted to a higher composition (occurring near 45% Zn) when compared to the 300 °C transition point. This may provide an explanation for the origin of the absorption band tails as these appear more strongly in the 400 °C films as seen in Figure 2g,h compared to Figure 2c,d. Enhanced absorption induced by greater structural disorder is typical of observed exponential Urbach tails.[105,106] These tails likely originate from additional "defects" propagating in the tin oxide matrix as more Zn is incorporated and strains the lattice. At the higher deposition temperature, a larger "defect" population is induced as the lattice is strained to incorporate a greater amount of Zn species and greater structural disorder. While oxygen vacancies have historically been implicated as the dominant defect in many oxide materials,[49] much of this composition range encompasses films with a disordered phase, meaning there cannot be oxygen vacancies. Instead, this absorption typically indicating enhanced disorder, in an already-disordered phase, may point to local distortions and changes in coordination, which have been discussed at length in the Ab Initio MD Simulations and Property Calculations section.

Hayashi et al. and Moriga et al. report a similar σ_e behavior[92,93] as the trend seen in Figure 3a. These two reports suggest the amorphous ZTO films are composed of $(ZnSnO_3)_{1−x}(SnO_2)_x$ over the range [Zn]/([Sn]+[Zn]) = ∼30–50% ($0 \leq x \leq 0.5$) and are composed of $(ZnSnO_3)_{1−y}(ZnO)_y$ over the range [Zn]/([Sn]+[Zn]) = ∼50–66.7% ($0 \leq y \leq 0.5$).[92,93] Moriga et al. posit that amorphization of the crystalline phase induces a significant increase in oxygen vacancy population, resulting in films with N_e up to 1×10^{20} cm$^{−3}$, similar to their crystalline bulk counterparts.[93] Upon reaching a saturation point, a reduction of carriers in the amorphous phase can be induced by either carrier compensation with Zn acting as an acceptor or due to increasing oxygen incorporation as greater amounts of ZnO are sputtered, which reduces the oxygen vacancy population.[93]

However, this picture is inconsistent with the oxygen concentration measured in the ZTO films of this study. Figure 4 shows the T_s = 400 °C films up to [Zn]/([Sn]+[Zn]) = 55.3% are overstoichiometric in oxygen (the film with maximum σ_e occurred at [Zn]/([Sn]+[Zn]) = 47.6% for T_s = 400 °C). Siah et al. has grown ZTO films at [Zn]/([Sn]+[Zn]) = 100, 78.8, 63.2, 35.7, and 0% whose measured oxygen contents, when compared to the red dashed curve in Figure 4, are similarly overstoichiometric.[11] Here, as greater amounts of ZnO are sputtered, the films become substoichiometric in oxygen. Specifically, this occurs when [Zn]/([Sn]+[Zn]) $\geq$ 68.2%, as observed in Figure 4. The dominant "defect" controlling the N_e, and subsequently the maximum σ_e, has to reconcile these observations.

A prior work in amorphous SnO has shown the propensity for the tin atoms to form stabilizing clusters, and become undercoordinated, upon amorphization.[107] Wahila et al. propose that these undercoordinated Sn atoms result in a valence band edge with a substantial metal s orbital character in the amorphous phase, producing subgap states in the disordered material, which allow enhancement of conduction properties. Wahila et al.,[72] Körner et al.,[68−70] and Rucavado et al.[71] demonstrate similar findings in amorphous ZTO, where subgap states are observed experimentally and theoretically to originate from local coordination changes of the cation and anion species.[72]

The present DFT-based MD results are indeed in agreement with the hard X-ray photoelectron spectroscopy (HAXPES) and DFT valence band calculations reported by Wahila et al.[72] However, Wahila et al. point to both a low Zn atomic % region and the 75−90% atomic Zn range as compositions for promising ZTO electrical behavior. These regions are both lower and higher than the [Zn]/([Sn]+[Zn]) where the highest σ_e occur for ZTO films shown in Figure 3a. It should be noted that Wahila et al. deposit ZTO films under differing conditions, namely, at room temperature, as compared to the 300 and 400 °C substrate temperatures of the films in Figure 3. Whereas Figure 3b show films with N_e = $10^{19}−10^{20}$, films characterized by Wahila et al. do not attain N_e higher than ∼10^{17}, as may be expected for lower temperature depositions. In the present study, peak σ_e shifts to a higher %Zn with increasing deposition temperature, occurring at 35.6% Zn for 300 °C films and 47.6% Zn for 400 °C films. This suggests a strong dependence of the formation of conduction chains with temperature and possibly high sensitivity to additional deposition conditions impacting local coordination.

These local distortions in coordination occur even in perfectly stoichiometric films.[72,108] The likelihood of under-coordinated Sn in the ZTO films studied here was highlighted in the Ab Initio MD Simulations and Property Calculations section and is consistent with prior works noted.[68−70,72,107] This leads us to propose a Frank−Köstlin-type associate as a candidate "defect" in this system: $2Sn_{Zn}^{\bullet\bullet}O_i''$. In tin-doped indium oxide, Frank and Köstlin proposed the existence of a neutral, reducible associate between tin donors and oxygen interstitials. This type of associate, now known as the Frank−Köstlin associate, has been the basis for defects proposed in both bulk and thin-film materials made in the $ZnO−In_2O_3−SnO_2$ (ZITO) system.[109,110]

In ZTO, the existence of $2Sn_{Zn}^{\bullet\bullet}O_i''$ would require Sn (4+) to replace a four-coordinated Zn (2+). The XRD spectra of Figure 1b,d provide evidence of significant amounts of ZnO in the amorphous films. From the MD simulated structures and Figure 5b, Zn strongly prefers to be four-coordinated even in amorphous structures. It must be emphasized that there is no lattice site for Sn to substitute for Zn in a strict sense as these films are amorphous. However, the MD simulated structures show a large portion of undercoordinated Sn in Figure 5a, suggesting that Sn atoms are located in four-coordinated positions.

Furthermore, the MD simulations strongly support Sn as the source of conduction electrons, consistent with a prior work in related amorphous oxide systems.[107] Figure 7b shows that Sn contributions to the charge density are significantly higher than those from Zn, even at 59% Zn incorporation into the ZTO structure. The calculated charge density near the Fermi level,

shown in Figure 7a, confirms that Sn states are indeed the source of carrier generation and transport.

CONCLUSIONS

ZTO films with compositions ranging across the entire ZnO–SnO$_2$ tie line were combinatorially sputtered. Structural analysis suggest a significant amount of ZnO fraction in the amorphous films, and MD simulated structures show that Zn in the amorphous phase has a strong tendency to be tetrahedrally coordinated by oxygen. Optical absorption in the sub-band gap region points to an increased defect population as Zn % is increased for films deposited at a higher substrate temperature. Contrary to conventional thought, oxygen vacancies are not the source of carriers as measured composition data show the films to be over-stoichiometric in oxygen in the region of highest carrier population. MD simulations show the tendency of Sn to be undercoordinated while simultaneously the source of carriers, suggesting a Frank–Köstlin-type defect present in the film, namely, $2Sn_{Zn}^{\bullet\bullet}O_i''$. Accurate calculations of the electronic properties of MD simulated amorphous Zn–Sn–O structures allow one to determine the cation fractional contribution to the density of states and charge density near the Fermi level, revealing that Sn contributes significantly more than Zn, further supporting the existence of both $2Sn_{Zn}^{\bullet\bullet}O_i''$ and Sn as the cation governing carrier generation. Furthermore, the simulated structures confirm that the Zn species control the medium-range structure and observed amorphous-to-crystalline or crystalline-to-amorphous transition points, i.e., Zn controls the morphology and subsequently the carrier mobility.

ASSOCIATED CONTENT

ⓈI Supporting Information

The Supporting Information is available free of charge at https://pubs.acs.org/doi/10.1021/acs.chemmater.0c01672.

> X-ray diffraction spectra of ZTO films grown at 300 °C over the composition range of [Zn]/([Sn]+[Zn]) = ∼9% to ∼76%; X-ray diffraction spectra of ZTO films grown at 400 °C over the composition range of [Zn]/([Sn]+[Zn]) = ∼9% to ∼76%; X-ray diffraction spectra of ZTO thin films with composition [Zn]/([Sn]+[Zn]) = 0–30.6% and 97.4–100%, deposited at 400 °C; X-ray diffraction spectra of [Zn]/([Sn]+[Zn]) = 76% taken with varied torsion angles, χ; calculated pair correlation functions for crystalline binary oxides and amorphous Zn–Sn–O; density of states calculations for non-stoichiometric amorphous structures of ZTO with 30, 44, and 59% atomic % Zn, all with one oxygen defect per cell; and calculated optical absorption for stoichiometric cases of amorphous ZTO structures with 30, 44, and 59% Zn (PDF)

AUTHOR INFORMATION

Corresponding Author

Mariana I. Bertoni − *Ira A. Fulton Schools of Engineering, Arizona State University, Tempe, Arizona 85287, United States;* orcid.org/0000-0002-0415-837X; Email: bertoni@asu.edu

Authors

Sebastian Husein − *Ira A. Fulton Schools of Engineering, Arizona State University, Tempe, Arizona 85287, United States;* orcid.org/0000-0003-2828-7392

Julia E. Medvedeva − *Department of Physics, Missouri S&T, Rolla, Missouri 65409, United States;* orcid.org/0000-0001-7142-1644

John D. Perkins − *National Renewable Energy Lab, Golden, Colorado 80401-3393, United States*

Complete contact information is available at:
https://pubs.acs.org/10.1021/acs.chemmater.0c01672

Notes

The authors declare no competing financial interest.

ACKNOWLEDGMENTS

REFERENCES

(1) Freeman, A. J.; Poeppelmeier, K. R.; Mason, T. O.; Chang, R. P.; Marks, T. J. Chemical and thin-film strategies for new transparent conducting oxides. *MRS Bull.* **2000**, *25*, 45−51.

(2) Ginley, D. S.; Bright, C. Transparent conducting oxides. *MRS Bull.* **2000**, *25*, 15−18.

(3) Barquinha, P.; Martins, R.; Pereira, L.; Fortunato, E. *Transparent Oxide Electronics: From Materials to Devices*; John Wiley & Sons: West Sussex, United Kingdom, 2012.

(4) Fortunato, E.; Ginley, D.; Hosono, H.; Paine, D. C. Transparent conducting oxides for photovoltaics. *MRS Bull.* **2007**, *32*, 242−247.

(5) Hosono, H. Ionic amorphous oxide semiconductors: Material design, carrier transport, and device application. *J. Non-Cryst. Solids* **2006**, *352*, 851−858.

(6) Nomura, K.; Ohta, H.; Takagi, A.; Kamiya, T.; Hirano, M.; Hosono, H. Room temperature fabrication of transparent flexible thin-film transistors using amorphous oxide semiconductors. *Nature* **2004**, *432*, 488−492.

(7) Kamiya, T.; Nomura, K.; Hosono, H. Origins of high mobility and low operation voltage of amorphous oxide TFTs: Electronic structure, electron transport, defects and doping. *J. Disp. Technol.* **2009**, *5*, 468−483.

(8) Walsh, A.; Da Silva, J. L. F.; Wei, S.-H. Interplay between order and disorder in the high performance of amorphous transparent conducting oxides. *Chem. Mater.* **2009**, *21*, 5119−5124.

(9) Kamiya, T.; Hosono, H. Material characteristics and applications of transparent amorphous oxide semiconductors. *NPG Asia Mater.* **2010**, *2*, 15−22.

(10) Sallis, S.; Butler, K. T.; Quackenbush, N. F.; Williams, D. S.; Junda, M.; Fischer, D. A.; Woicik, J.; Podraza, N. J.; White, B. E., Jr.; Walsh, A.; Piper, L. F. J. Origin of deep subgap states in amorphous indium gallium zinc oxide: Chemically disordered coordination of oxygen. *Appl. Phys. Lett.* **2014**, *104*, 232108.

(11) Siah, S. C.; Lee, S. W.; Lee, Y. S.; Heo, J.; Shibata, T.; Segre, C. U.; Gordon, R. G.; Buonassisi, T. X-ray absorption spectroscopy elucidates the impact of structural disorder on electron mobility in

amorphous zinc-tin-oxide thin films. *Appl. Phys. Lett.* **2014**, *104*, 242113.

(12) Khanal, R.; Buchholz, D. B.; Chang, R. P.; Medvedeva, J. E. Composition-dependent structural and transport properties of amorphous transparent conducting oxides. *Phys. Rev. B* **2015**, *91*, 205203.

(13) Niang, K. M.; Cho, J.; Heffernan, S.; Milne, W. I.; Flewitt, A. J. Optimisation of amorphous zinc tin oxide thin film transistors by remote-plasma reactive sputtering. *J. Appl. Phys.* **2016**, *120*, No. 085312.

(14) Medvedeva, J. E.; Buchholz, D. B.; Chang, R. P. H. Recent advances in understanding the structure and properties of amorphous oxide semiconductors. *Adv. Electron. Mater.* **2017**, *3*, 1700082.

(15) Ryu, M. K.; Yang, S.; Park, S.-H. K.; Hwang, C.-S.; Jeong, J. K. High performance thin film transistor with cosputtered amorphous Zn−In−Sn−O channel: Combinatorial approach. *Appl. Phys. Lett.* **2009**, *95*, No. 072104.

(16) Taylor, M. P.; Readey, D. W.; van Hest, M. F. A. M.; Teplin, C. W.; Alleman, J. L.; Dabney, M. S.; Gedvilas, L. M.; Keyes, B. M.; To, B.; Perkins, J. D.; Ginley, D. S. The Remarkable Thermal Stability of Amorphous In-Zn-O Transparent Conductors. *Adv. Funct. Mater.* **2008**, *18*, 3169−3178.

(17) Morales-Masis, M.; Dauzou, F.; Jeangros, Q.; Dabirian, A.; Lifka, H.; Gierth, R.; Ruske, M.; Moet, D.; Hessler-Wyser, A.; Ballif, C. An Indium-Free Anode for LargeArea Flexible OLEDs: Defect-Free Transparent Conductive Zinc Tin Oxide. *Adv. Funct. Mater.* **2016**, *26*, 384−392.

(18) Chae, G. S. A modified transparent conducting oxide for flat panel displays only. *Jpn. J. Appl. Phys.* **2001**, *40*, 1282.

(19) Ito, M.; Kon, M.; Miyazaki, C.; Ikeda, N.; Ishizaki, M.; Matsubara, R.; Ugajin, Y.; Sekine, N. Amorphous oxide TFT and their applications in electrophoretic displays. *Phys. Status Solidi A* **2008**, *205*, 1885−1894.

(20) Wang, L.; Yoon, M.-H.; Lu, G.; Yang, Y.; Facchetti, A.; Marks, T. J. High-performance transparent inorganic−organic hybrid thin-film n-type transistors. *Nat. Mater.* **2006**, *5*, 893−900.

(21) Yu, X.; Marks, T. J.; Facchetti, A. Metal oxides for optoelectronic applications. *Nat. Mater.* **2016**, *15*, 383−396.

(22) Bellingham, J. R.; Phillips, W. A.; Adkins, C. J. Electrical and optical properties of amorphous indium oxide. *J. Phys.: Condens. Matter* **1990**, *2*, 6207.

(23) Shigesato, Y.; Paine, D. C. Study of the effect of Sn doping on the electronic transport properties of thin film indium oxide. *Appl. Phys. Lett.* **1993**, *62*, 1268−1270.

(24) Ito, N.; Sato, Y.; Song, P.; Kaijio, A.; Inoue, K.; Shigesato, Y. Electrical and optical properties of amorphous indium zinc oxide films. *Thin Solid Films* **2006**, *496*, 99−103.

(25) Nakazawa, H.; Ito, Y.; Matsumoto, E.; Adachi, K.; Aoki, N.; Ochiai, Y. The electronic properties of amorphous and crystallized In_2O_3 films. *J. Appl. Phys.* **2006**, *100*, No. 093706.

(26) Martins, R.; Barquinha, P.; Pimentel, A.; Pereira, L.; Fortunato, E. Transport in high mobility amorphous wide band gap indium zinc oxide films. *Phys. Status Solidi A* **2005**, *202*, R95−R97.

(27) Chiang, H.; Wager, J. F.; Hoffman, R. L.; Jeong, J.; Keszler, D. A. High mobility transparent thin-film transistors with amorphous zinc tin oxide channel layer. *Appl. Phys. Lett.* **2005**, *86*, No. 013503.

(28) Yabuta, H.; Sano, M.; Abe, K.; Aiba, T.; Den, T.; Kumomi, H.; Nomura, K.; Kamiya, T.; Hosono, H. High-mobility thin-film transistor with amorphous $In Ga Zn O_4$ channel fabricated by room temperature rf-magnetron sputtering. *Appl. Phys. Lett.* **2006**, *89*, 112123.

(29) Jeong, J. K.; Jeong, J. H.; Yang, H. W.; Park, J.-S.; Mo, Y.-G.; Kim, H. D. High performance thin film transistors with cosputtered amorphous indium gallium zinc oxide channel. *Appl. Phys. Lett.* **2007**, *91*, 113505.

(30) Emmer, H.; Chen, C. T.; Saive, R.; Friedrich, D.; Horie, Y.; Arbabi, A.; Faraon, A.; Atwater, H. A. Fabrication of single crystal gallium phosphide thin films on glass. *Sci. Rep.* **2017**, *7*, 4643.

(31) Leenheer, A. J.; Perkins, J. D.; Van Hest, M. F.; Berry, J. J.; O'Hayre, R. P.; Ginley, D. S. General mobility and carrier concentration relationship in transparent amorphous indium zinc oxide films. *Phys. Rev. B* **2008**, *77*, 115215.

(32) Kim, M.-G.; Kim, H. S.; Ha, Y.-G.; He, J.; Kanatzidis, M. G.; Facchetti, A.; Marks, T. J. High-performance solution-processed amorphous zinc-indium-tin oxide thin-film transistors. *J. Am. Chem. Soc.* **2010**, *132*, 10352−10364.

(33) Kuznetsov, V. L.; O'Neil, D. H.; Pepper, M.; Edwards, P. P. Electronic conduction in amorphous and polycrystalline zinc-indium oxide films. *Appl. Phys. Lett.* **2010**, *97*, 262117.

(34) Jeong, S.; Ha, Y.-G.; Moon, J.; Facchetti, A.; Marks, T. J. Role of gallium doping in dramatically lowering amorphous-oxide processing temperatures for solution-derived indium zinc oxide thin-film transistors. *Adv. Mater.* **2010**, *22*, 1346−1350.

(35) Lee, J.; Cho, D.-Y.; Jung, J.; Ki Kim, U.; Ho Rha, S.; Seong Hwang, C.; Choi, J.-H. Theoretical and experimental studies on the electronic structure of crystalline and amorphous $ZnSnO_3$ thin films. *Appl. Phys. Lett.* **2013**, *102*, 242111.

(36) Buchholz, D. B.; Ma, Q.; Alducin, D.; Ponce, A.; Jose-Yacaman, M.; Khanal, R.; Medvedeva, J. E.; Chang, R. P. The structure and properties of amorphous indium oxide. *Chem. Mater.* **2014**, *26*, 5401−5411.

(37) Liu, C. P.; Ho, C. Y.; Kwok, C. K.; Guo, P. F.; Hossain, M. K.; Zapien, J. A.; Yu, K. M. High mobility transparent amorphous CdO-In_2O_3 alloy films synthesized at room temperature. *Appl. Phys. Lett.* **2017**, *111*, No. 072108.

(38) Koida, T.; Kondo, M.; Tsutsumi, K.; Sakaguchi, A.; Suzuki, M.; Fujiwara, H. Hydrogen-doped In_2O_3 transparent conducting oxide films prepared by solid-phase crystallization method. *J. Appl. Phys.* **2010**, *107*, No. 033514.

(39) Husein, S.; Stuckelberger, M.; West, B.; Ding, L.; Dauzou, F.; Morales-Masis, M.; Duchamp, M.; Holman, Z.; Bertoni, M. I. Carrier scattering mechanisms limiting mobility in hydrogen-doped indium oxide. *J. Appl. Phys.* **2018**, *123*, 245102.

(40) Jayaraj, M. K.; Saji, K. J.; Nomura, K.; Kamiya, T.; Hosono, H. Optical and electrical properties of amorphous zinc tin oxide thin films examined for thin film transistor application. *J. Vac. Sci. Technol., B: Microelectron. Nanometer Struct.–Process., Meas., Phenom.* **2008**, *26*, 495−501.

(41) Kılıç, Ç.; Zunger, A. *n*-type doping of oxides by hydrogen. *Appl. Phys. Lett.* **2002**, *81*, 73−75.

(42) Janotti, A.; Van de Walle, C. G. Hydrogen multicentre bonds. *Nat. Mater.* **2007**, *6*, 44−47.

(43) Cox, S. F. J.; Davis, E. A.; Cottrell, S. P.; King, P. J. C.; Lord, J. S.; Gil, J. M.; Alberto, H. V.; Vilão, R. C.; Duarte, J. P.; de Campos, N. A.; Weidinger, A.; Lichti, R. L.; Irvine, S. J. C. Experimental confirmation of the predicted shallow donor hydrogen state in zinc oxide. *Phys. Rev. Lett.* **2001**, *86*, 2601.

(44) Hofmann, D. M.; Hofstaetter, A.; Leiter, F.; Zhou, H.; Henecker, F.; Meyer, B. K.; Orlinskii, S. B.; Schmidt, J.; Baranov, P. G. Hydrogen: a relevant shallow donor in zinc oxide. *Phys. Rev. Lett.* **2002**, *88*, No. 045504.

(45) Saive, R.; Mueller, L.; Mankel, E.; Kowalsky, W.; Kroeger, M. Doping of TIPSpentacene via Focused Ion Beam (FIB) exposure. *Org. Electron.* **2013**, *14*, 1570−1576.

(46) King, P. D. C.; Lichti, R. L.; Celebi, Y. G.; Gil, J. M.; Vilão, R. C.; Alberto, H. V.; Duarte, J. P.; Payne, D. J.; Egdell, R. G.; McKenzie, I.; McConville, C. F.; Cox, S. F. J.; Veal, T. D. Shallow donor state of hydrogen in In_2O_3 and SnO_2: Implications for conductivity in transparent conducting oxides. *Phys. Rev. B* **2009**, *80*, No. 081201.

(47) Limpijumnong, S.; Reunchan, P.; Janotti, A.; Van de Walle, C. G. Hydrogen doping in indium oxide: An *ab initio* study. *Phys. Rev. B* **2009**, *80*, 193202.

(48) Varley, J. B.; Weber, J. R.; Janotti, A.; Van de Walle, C. G. Oxygen vacancies and donor impurities in β-Ga_2O_3. *Appl. Phys. Lett.* **2010**, *97*, 142106.

(49) King, P. D. C.; Veal, T. D. Conductivity in transparent oxide semiconductors. *J. Phys.: Condens. Matter* **2011**, *23*, 334214.

(50) Macco, B.; Knoops, H. C. M.; Kessels, W. M. M. Electron scattering and doping mechanisms in solid-phase-crystallized In$_2$O$_3$: H prepared by atomic layer deposition. *ACS Appl. Mater. Interfaces* **2015**, *7*, 16723−16729.

(51) Muydinov, R.; Steigert, A.; Wollgarten, M.; Michałowski, P. P.; Bloeck, U.; Pflug, A.; Erfurt, D.; Klenk, R.; Körner, S.; Lauermann, I.; Szyszka, B. Crystallisation Phenomena of In$_2$O$_3$: H Films. *Materials* **2019**, *12*, 266.

(52) Nakamura, E.; Sato, K. Managing the scarcity of chemical elements. *Nat. Mater.* **2011**, *10*, 158−161.

(53) Candelise, C.; Speirs, J. F.; Gross, R. J. K. Materials availability for thin film (TF) PV technologies development: a real concern? *Renewable Sustainable Energy Rev.* **2011**, *15*, 4972−4981.

(54) Jackson, W. B.; Hoffman, R. L.; Herman, G. S. High-performance flexible zinc tin oxide field effect transistors. *Appl. Phys. Lett.* **2005**, *87*, 193503.

(55) Heineck, D. P.; McFarlane, B. R.; Wager, J. F. Zinc tin oxide thin-film-transistor enhancement/depletion inverter. *IEEE Electron Device Lett.* **2009**, *30*, 514−516.

(56) Nayak, P. K.; Pinto, J. V.; Gonçalves, G.; Martins, R.; Fortunato, E. Environmental, optical, and electrical stability study of solution-processed zinc−tin−oxide thin-film transistors. *J. Disp. Technol.* **2011**, *7*, 640−643.

(57) Oo, T. Z.; Chandra, R. D.; Yantara, N.; Prabhakar, R. R.; Wong, L. H.; Mathews, N.; Mhaisalkar, S. G. Zinc Tin Oxide (ZTO) electron transporting buffer layer in inverted organic solar cell. *Org. Electron.* **2012**, *13*, 870−874.

(58) Weigel, C. S.; Kowalsky, W.; Saive, R. Direct observation of the potential distribution within organic light emitting diodes under operation. *Phys. Status Solidi Rapid Res. Lett.* **2015**, *9*, 475−479.

(59) Saive, R. S-Shaped Current−Voltage Characteristics in Solar Cells: A Review. *IEEE J. Photovoltaics* **2019**, *9*, 1477−1484.

(60) Lindahl, J.; Wätjen, J. T.; Hultqvist, A.; Ericson, T.; Edoff, M.; Törndahl, T. The effect of Zn$_{1-x}$ Sn$_x$ O$_y$ buffer layer thickness in 18.0% efficient Cd-free Cu (In, Ga)Se$_2$ solar cells. *Progr. Photovolt.: Res. Appl.* **2013**, *21*, 1588−1597.

(61) Lee, Y. S.; Heo, J.; Siah, S. C.; Mailoa, J. P.; Brandt, R. E.; Kim, S. B.; Gordon, R. G.; Buonassisi, T. Ultrathin amorphous zinc-tin-oxide buffer layer for enhancing heterojunction interface quality in metal-oxide solar cells. *Energy Environ. Sci.* **2013**, *6*, 2112−2118.

(62) Lee, C.-G.; Dodabalapur, A. Solution-processed zinc−tin oxide thin-film transistors with low interfacial trap density and improved performance. *Appl. Phys. Lett.* **2010**, *96*, 243501.

(63) Wang, C.-H.; Chen, S.-W.; Wu, J.-M.; Wei, C.-N.; Bor, H.-Y. Effect of postdeposition oxidation and subsequent reduction annealing on electric and optical properties of amorphous ZnO−SnO$_2$ transparent conducting films. *Electrochem. Solid-State Lett.* **2011**, *14*, P5−P8.

(64) Choi, Y.-Y.; Kang, S. J.; Kim, H.-K. Rapid thermal annealing effect on the characteristics of ZnSnO$_3$ films prepared by RF magnetron sputtering. *Curr. Appl. Phys.* **2012**, *12*, S104−S107.

(65) Chang, Y.-J.; Lee, D.-H.; Herman, G. S.; Chang, C.-H. High-performance, spin-coated zinc tin oxide thin-film transistors. *Electrochem. Solid-State Lett.* **2007**, *10*, H135−H138.

(66) Seo, S.-J.; Choi, C. G.; Hwang, Y. H.; Bae, B.-S. High performance solution-processed amorphous zinc tin oxide thin film transistor. *J. Phys. D: Appl. Phys.* **2008**, *42*, No. 035106.

(67) Chen, Y.-C.; Chang, T.-C.; Li, H.-W.; Chung, W.-F.; Wu, C.-P.; Chen, S.-C.; Lu, J.; Chen, Y.-H.; Tai, Y.-H. High-stability oxygen sensor based on amorphous zinc tin oxide thin film transistor. *Appl. Phys. Lett.* **2012**, *100*, 262908.

(68) Körner, W.; Gumbsch, P.; Elsässer, C. Analysis of electronic subgap states in amorphous semiconductor oxides based on the example of Zn-Sn-O systems. *Phys. Rev. B* **2012**, *86*, 165210.

(69) Körner, W.; Urban, D. F.; Ramo, D. M.; Bristowe, P. D.; Elsässer, C. Prediction of subgap states in Zn-and Sn-based oxides using various exchange-correlation functionals. *Phys. Rev. B* **2014**, *90*, 195142.

(70) Körner, W.; Elsässer, C. Density-functional theory study of stability and subgap states of crystalline and amorphous Zn−Sn−O. *Thin Solid Films* **2014**, *555*, 81−86.

(71) Rucavado, E.; Jeangros, Q.; Urban, D. F.; Holovsky, J.; Remes, Z.; Duchamp, M.; Landucci, F.; Dunin-Borkowski, R. E.; Körner, W.; Elsässer, C.; Hessler-Wyser, A.; Morales-Masis, M.; Ballif, C. Enhancing the optoelectronic properties of amorphous zinc tin oxide by subgap defect passivation: A theoretical and experimental demonstration. *Phys. Rev. B* **2017**, *95*, 245204.

(72) Wahila, M. J.; Lebens-Higgins, Z. W.; Butler, K. T.; Fritsch, D.; Treharne, R. E.; Palgrave, R. G.; Woicik, J. C.; Morgan, B. J.; Walsh, A.; Piper, L. F. J. Accelerated optimization of transparent, amorphous zinc-tin-oxide thin films for optoelectronic applications. *APL Mater.* **2019**, *7*, No. 022509.

(73) Zhussupbekova, A.; Kaisha, A.; Vijayaraghavan, R. K.; Fleischer, K.; Shvets, I. V.; Caffrey, D. The importance of local bond order to conduction in amorphous, transparent, conducting oxides: The case of amorphous ZnSnO$_y$. *ACS Appl. Mater. Interfaces* **2019**, *11*, 44399−44405.

(74) Young, D. L.; Williamson, D. L.; Coutts, T. J. Structural characterization of zinc stannate thin films. *J. Appl. Phys.* **2002**, *91*, 1464−1471.

(75) Young, D. L.; Moutinho, H.; Yan, Y.; Coutts, T. J. Growth and characterization of radio frequency magnetron sputter-deposited zinc stannate, Zn$_2$SnO$_4$, thin films. *J. Appl. Phys.* **2002**, *92*, 310−319.

(76) Wu, X.; Coutts, T.; Mulligan, W. Properties of transparent conducting oxides formed from CdO and ZnO alloyed with SnO$_2$ and In$_2$O$_3$. *J. Vac. Sci. Technol., A* **1997**, *15*, 1057−1062.

(77) Sun, S.; Liang, S. Morphological zinc stannate: synthesis, fundamental properties and applications. *J. Mater. Chem. A* **2017**, *5*, 20534−20560.

(78) Pankove, J. I. *Optical Processes in Semiconductors*; Courier Corporation: Golden, Colorado, USA, 1975.

(79) Kresse, G.; Hafner, J. *Ab initio* molecular dynamics for liquid metals. *Phys. Rev. B* **1993**, *47*, 558−561.

(80) Kresse, G.; Furthmüller, J.; Hafner, J. Theory of the crystal structures of selenium and tellurium: the effect of generalized-gradient corrections to the local-density approximation. *Phys. Rev. B* **1994**, *50*, 13181.

(81) Kresse, G.; Furthmüller, J. Efficiency of ab-initio total energy calculations for metals and semiconductors using a plane-wave basis set. *Comput. Mater. Sci.* **1996**, *6*, 15−50.

(82) Kresse, G.; Furthmüller, J. Efficient iterative schemes for *ab initio* total-energy calculations using a plane-wave basis set. *Phys. Rev. B* **1996**, *54*, 11169.

(83) Hafner, J. Materials simulations using VASP—a quantum perspective to materials science. *Comput. Phys. Commun.* **2007**, *177*, 6−13.

(84) Perdew, J. P.; Burke, K.; Ernzerhof, M. Generalized gradient approximation made simple. *Phys. Rev. Lett.* **1996**, *77*, 3865.

(85) Hoppe, R. The Coordination Number − an "Inorganic Chameleon". *Angew. Chem., Int. Ed. Engl.* **1970**, *9*, 25−34.

(86) Hoppe, R.; Voigt, S.; Glaum, H.; Kissel, J.; Müller, H. P.; Bernet, K. A new route to charge distributions in ionic solids. *J. Less-Common Met.* **1989**, *156*, 105−122.

(87) Medvedeva, J. E.; Khanal, R. Long-range structural correlations in amorphous ternary In-based oxides. *Vacuum* **2015**, *114*, 142−149.

(88) Heyd, J.; Scuseria, G. E.; Ernzerhof, M. Hybrid functionals based on a screened Coulomb potential. *J. Chem. Phys.* **2003**, *118*, 8207−8215.

(89) Heyd, J.; Peralta, J. E.; Scuseria, G. E.; Martin, R. L. Energy band gaps and lattice parameters evaluated with the Heyd-Scuseria-Ernzerhof screened hybrid functional. *J. Chem. Phys.* **2005**, *123*, 174101.

(90) Tang, W.; Sanville, E.; Henkelman, G. A grid-based Bader analysis algorithm without lattice bias. *J. Phys.: Condens. Matter* **2009**, *21*, No. 084204.

(91) Momma, K.; Izumi, F. VESTA 3 for three-dimensional visualization of crystal, volumetric and morphology data. *J. Appl. Crystallogr.* **2011**, *44*, 1272−1276.

(92) Hayashi, Y.; Kondo, K.; Murai, K.; Moriga, T.; Nakabayashi, I.; Fukumoto, H.; Tominaga, K. ZnO−SnO$_2$ transparent conductive films deposited by opposed target sputtering system of ZnO and SnO$_2$ targets. *Vacuum* **2004**, *74*, 607−611.

(93) Moriga, T.; Hayashi, Y.; Kondo, K.; Nishimura, Y.; Murai, K. i.; Nakabayashi, I.; Fukumoto, H.; Tominaga, K. Transparent conducting amorphous Zn−Sn−O films de posited by simultaneous dc sputtering. *J. Vac. Sci. Technol., A* **2004**, *22*, 1705−1710.

(94) Fröhlich, D.; Kenklies, R.; Helbig, R. Band-Gap Assignment in SnO$_2$ by Two-Photon Spectroscopy. *Phys. Rev. Lett.* **1978**, *41*, 1750.

(95) Mishra, K. C.; Johnson, K. H.; Schmidt, P. C. Electronic structure of antimony-doped tin oxide. *Phys. Rev. B* **1995**, *51*, 13972.

(96) Barbarat, P.; Matar, S. F.; Blevennec, G. L. First-principles investigations of the electronic, optical and chemical bonding properties of SnO$_2$. *Comput. Mater. Sci.* **1998**, *10*, 368−372.

(97) Minami, T. Transparent and conductive multicomponent oxide films prepared by magnetron sputtering. *J. Vac. Sci. Technol., A* **1999**, *17*, 1765−1772.

(98) Kucheyev, S. O.; Baumann, T. F.; Sterne, P. A.; Wang, Y. M.; van Buuren, T.; Hamza, A. V.; Terminello, L. J.; Willey, T. M. Surface electronic states in three-dimensional SnO$_2$ nanostructures. *Phys. Rev. B* **2005**, *72*, No. 035404.

(99) Schleife, A.; Varley, J. B.; Fuchs, F.; Rödl, C.; Bechstedt, F.; Rinke, P.; Janotti, A.; Van de Walle, C. G. Tin dioxide from first principles: Quasiparticle electronic states and optical properties. *Phys. Rev. B* **2011**, *83*, No. 035116.

(100) Das, S.; Jayaraman, V. SnO$_2$: A comprehensive review on structures and gas sensors. *Prog. Mater. Sci.* **2014**, *66*, 112−255.

(101) Schulz, H.; Thiemann, K. H. Crystal structure refinement of AlN and GaN. *Solid State Commun.* **1977**, *23*, 815−819.

(102) Perkins, J. D.; del Cueto, J. A.; Alleman, J. L.; Warmsingh, C.; Keyes, B. M.; Gedvilas, L. M.; Parilla, P. A.; To, B.; Readey, D. W.; Ginley, D. S. Combinatorial studies of Zn-Al-O and Zn-Sn-O transparent conducting oxide thin films. *Thin Solid Films* **2002**, *411*, 152−160.

(103) Janotti, A.; Van de Walle, C. G. Native point defects in ZnO. *Phys. Rev. B* **2007**, *76*, 165202.

(104) Fujita, S. Wide-bandgap semiconductor materials: For their full bloom. *Jpn. J. Appl. Phys.* **2015**, *54*, No. 030101.

(105) John, S.; Soukoulis, C.; Cohen, M. H.; Economou, E. N. Theory of electron band tails and the Urbach optical-absorption edge. *Phys. Rev. Lett.* **1986**, *57*, 1777.

(106) Bonalde, I.; Medina, E.; Rodríguez, M.; Wasim, S. M.; Marín, G.; Rincón, C.; Rincón, A.; Torres, C. Urbach tail, disorder, and localized modes in ternary semiconductors. *Phys. Rev. B* **2004**, *69*, 195201.

(107) Wahila, M. J.; et al. Lone-pair stabilization in transparent amorphous tin oxides: a potential route to p-type conduction pathways. *Chem. Mater.* **2016**, *28*, 4706−4713.

(108) Medvedeva, J. E.; Zhuravlev, I. A.; Burris, C.; Buchholz, D. B.; Grayson, M.; Chang, R. P. H. Origin of high carrier concentration in amorphous wide-bandgap oxides: Role of disorder in defect formation and electron localization in In$_2$O$_3$-x. *J. Appl. Phys.* **2020**, *127*, 175701.

(109) Ambrosini, A.; Malo, S.; Poeppelmeier, K. R.; Lane, M. A.; Kannewurf, C. R.; Mason, T. O. Zinc Doping in Cosubstituted In$_{2-2x}$Sn$_x$Zn$_x$O$_{3-\delta}$. *Chem. Mater.* **2002**, *14*, 58−63.

(110) Harvey, S. P.; Mason, T. O.; Buchholz, D. B.; Chang, R. P. H.; Körber, C.; Klein, A. Carrier Generation and Inherent Off-Stoichiometry in Zn, Sn Codoped Indium Oxide (ZITO) Bulk and Thin-Film Specimens. *J. Am. Ceram. Soc.* **2008**, *91*, 467−472.